

High Permittivity $(1 - x)\text{Ba}(\text{Zr}_{0.2}\text{Ti}_{0.8})\text{O}_3 - x(\text{Ba}_{0.7}\text{Ca}_{0.3})\text{TiO}_3$ ($x = 0.45$) Epitaxial Thin Films with Nanoscale Phase Fluctuations

Nicu D. Scarisoreanu,^{*,†} Floriana Craciun,[‡] Antoniu Moldovan,[†] Valentin Ion,[†] Ruxandra Birjega,[†] Cornelius Ghica,[§] Raluca F. Negrea,[§] and Maria Dinescu[†]

[†]National Institute for Laser, Plasma and Radiation Physics, 409 Atomistilor, 077125 Magurele, Romania

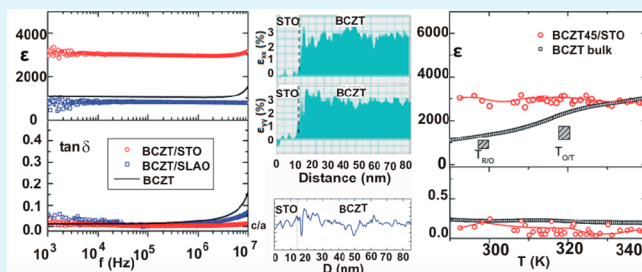
[‡]CNR-ISC, Istituto dei Sistemi Complessi, Area della Ricerca di Roma-Tor Vergata, Via del Fosso del Cavaliere 100, I-00133, Rome, Italy

[§]National Institute of Materials Physics, 105 bis Atomistilor, 077125 Magurele, Romania

Supporting Information

ABSTRACT: Epitaxial $(1 - x)\text{Ba}(\text{Zr}_{0.2}\text{Ti}_{0.8})\text{O}_3 - x(\text{Ba}_{0.7}\text{Ca}_{0.3})\text{TiO}_3$, $x = 0.45$ (BCZT 45), thin films have been deposited on (001) SrTiO_3 (STO) and (001/100) SrLaAlO_4 (SLAO) substrates by pulsed laser deposition. X-ray diffraction and high-resolution transmission electron microscopy (HRTEM) confirmed the epitaxial growth of the films. A high structural quality has been evidenced for the BCZT/STO films. Geometric phase analysis (GPA) associated with the HRTEM enabled us to obtain microstrain analysis and the in-plane and out-of-plane lattice parameter variation on different areas. Tetragonality ratio fluctuations at nanoscale level which are relevant for the existence of nanodomains have been evidenced on the BCZT/STO films. The in-plane dielectric constant has been measured on interdigital electrodes deposited by lift-off technique on the top of the films. High values of dielectric permittivity (>3000) combined with low dielectric loss (<0.01) are obtained for BCZT 45 film deposited on STO substrate, showing nearly constant values between 1 kHz and 10 MHz. The high dielectric permittivity of BCZT thin films was attributed to their high structural quality and to the loss of rotation stability of the polarization associated with the presence of nanodomains. This results into a divergence of fluctuations of polarization direction and a peak of dielectric susceptibility. The enhanced switching of such nanodomain configuration was probed by piezoforce microscopy, by writing and reading domains during topography scanning.

KEYWORDS: BCZT thin films, HRTEM, geometric phase analysis, dielectric permittivity, piezoforce microscopy



1. INTRODUCTION

Due to its large piezoelectric response, BaTiO_3 (BT) ferroelectric perovskite is commonly used to develop new lead-free piezoelectric materials. The ferroelectricity in this compound originates from the Ti^{4+} ion shift in the BO_6 octahedron, giving rise to three ferroelectric phases: tetragonal (T) with space group $P4mm$ (stable between 390 and 265 K) with spontaneous polarization $P_s \parallel (001)$, orthorhombic (O) with space group $Amm2$ (stable between 265 and 180 K) with $P_s \parallel (011)$, and rhombohedral (R) with space group $R3m$ (stable below 180 K) with $P_s \parallel (111)$.¹ However, in pure BT, these three phases are very different in free energy and separated by large temperature intervals. Moreover the T–O and O–R phase transitions occur below room temperature. Therefore, A- and/or B- site substitutions have been employed in order to bring these phase transitions closer to each other and near room temperature. The most interesting results have been obtained by substituting Zr^{4+} for Ti^{4+} and Ca^{2+} for Ba^{2+} .^{1–9} Thus, it has been shown that polymorphic phase boundaries and enhanced piezoelectric response can be obtained by substituting larger ionic radius Zr^{4+} (0.72 Å) in

place of Ti^{4+} (0.605 Å), which favors oxygen octahedra tilting.¹ The ferroelectric transition temperature T_c decreases while T_{T-O} and T_{R-O} increase with Zr concentration, and they all converge at a temperature of 340 K for Zr content 15 mol %. The detailed structural analysis showed that the composition range where enhanced dielectric and piezoelectric properties are found is characterized by coexistence of two (R+O or O+T) ferroelectric phases. The response can be further enhanced by substituting smaller Ca^{2+} ions for Ba^{2+} in $\text{Ba}(\text{Zr},\text{Ti})\text{O}_3$ as shown in refs.,^{2,9} since this substitution brings the different phase transitions of $\text{Ba}(\text{Zr},\text{Ti})\text{O}_3$ in the room temperature range. The mechanism is related to the large difference between the ionic radii of Ba^{2+} (1.61 Å) and Ca^{2+} (1.34 Å); the chemical pressure due to unit cell reduction in $(\text{Ba},\text{Ca})(\text{Zr},\text{Ti})\text{O}_3$ influences the phase transition temperature similarly to hydrostatic pressure, that is T_{T-O} and T_{R-O} show a continuous decrease down to the lowest temperatures.¹⁰ However, T_c is nearly independent,

Received: July 24, 2015

Accepted: October 13, 2015

Published: October 13, 2015

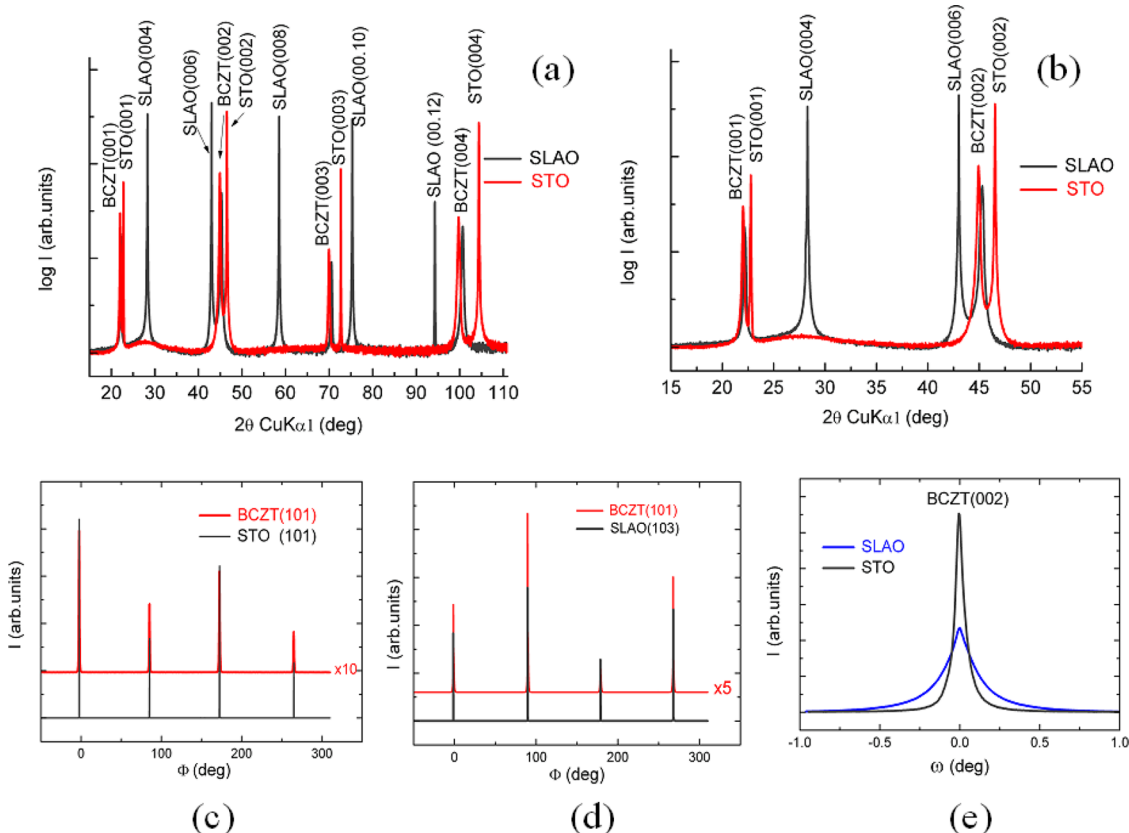


Figure 1. (a) XRD patterns of the BCZT/STO and BCZT/SLAO heterostructures; (b) detailed XRD patterns in the first half of the recorded angular range; (c) 360° φ -scans of BCZT (101) and STO (101) asymmetric reflections; (d) 360° φ -scans of BCZT (101) and SLAO(103) reflections; and (e) ω -scans of symmetric reflections.

which means that a new polarization component acts in these compounds to compensate for the pressure-induced instability. Indeed, first-principles calculations showed that the small Ca²⁺ cations incorporated in the host lattice tend to locate at an off-centering position.⁹ Thus, the additional polarization originates from this off-center displacement of smaller Ca ions at the Ba site, which works cooperatively with Ti–O distortion.

The ferroelectric distortions of the T, O, and R phases in (Ba,Ca)(Zr,Ti)O₃ compounds are very small, and moreover, the difference of R–O and O–R transition temperatures is about 10 K, indicating that the free energy difference between these ferroelectric phases is very small. The stabilization of the two polymorphic phase boundary regions near room temperature in these compounds, which is the origin of their high dielectric and piezoelectric response, is favored by three factors: the first-order nature of the phase transitions, the increased coexistence range due to random elastic strain associated with substitutions, and the shift of transition temperatures toward room temperature with Zr and Ca substitutions.

The phase diagram of (Ba,Ca)(Zr,Ti)O₃ compounds has been rationalized in terms of two end-members, Zr-doped BT and Ca-doped BT, and the most investigated compositions belong to the pseudobinary phase diagram $(1-x)\text{Ba}-(\text{Zr}_{0.2}\text{Ti}_{0.8})\text{O}_3 - x(\text{Ba}_{0.7}\text{Ca}_{0.3})\text{TiO}_3$ (BCZT 100x).^{2–8} The symmetry of the O phase in BCZT has been found to be *Amm*2, like in BT.³ Rietveld refinements confirmed that the phase symmetry sequence observed in BCZT with temperature decreasing is *Pm3m*–*P4mm*–*Amm*2–*R3m*, similar to that observed in BTO.³

Thus, maximizing the number of coexisting phases at room temperature was found to be the main route to enhance the dielectric and piezoelectric response in BCZT solid solutions. However, this can be achieved not only by substitutions but also by tailoring the space of constraints (epitaxial strain, pressure, electric field etc.),¹¹ so that phase diagrams with multiple dimensions, as e.g. $T-\sigma_1-\sigma_2-E_i-x(\text{Ba,Ca})\text{TiO}_3-y\text{Ba}(\text{Zr,Ti})\text{O}_3$ can be considered. Indeed, it has been shown that a large contribution to the mechanical or electrical response comes from the entropy increase due to coexistence of paraelectric cubic, R, O, T, and eventually other low symmetry phases, like monoclinic, with local polarization directions randomly distributed along allowed symmetry directions.¹¹ Thus, by engineering the material system so that it can be operated near the invariant critical point to maximize the number of coexisting phases and, consequently, the entropy, a very large dielectric and electromechanical response may be realized.¹¹ The ways open by strain engineering in thin films can thus be fruitfully applied in BCZT thin films, to maximize the number of coexistent competing phases.

A remarkable feature of these systems is the potential to transform their ground states under an applied mechanical constraint. For example, when a large compressive strain occurs in a thin film due to the epitaxial constraint from the underlying substrate, the ground state R transforms into a T-like (or O-like) phase.¹² Moreover, when the epitaxial constraint is partially relaxed by increasing the film thickness, this T phase evolves into a state consisting of a nanoscale mixture of the R-like phase embedded into the T-like phase.¹² Similar effects have been reported in SrRuO₃ thin films grown in epitaxial

Table 1. Structural Data Extracted from XRD and HRTEM Analysis

film on substrate	TEM Results				calcd a_p (nm) in-plane in BCZT	calcd a_n (nm) out-of-plane in BCZT			
	ε_{xx} in BCZT with respect to substrate (%)	ε_{yy} in BCZT with respect to substrate (%)							
STO	2.8 ± 0.4		2.9 ± 0.3		0.4014 ± 0.0016	0.4018 ± 0.0012			
SLAO	5.3 ± 0.6		-3.1 ± 0.8		0.3955 ± 0.0024	0.4081 ± 0.032			
XRD results									
film on substrate	lattice parameters		strain due to misfit with the substrate		rocking	Williamson–Hall analysis			
	a_p (nm) in plane	a_n (nm) out of plane	ε_{xx} in plane (%)	ε_{yy} out of plane (%)	curve (002) (deg)	D_\perp (nm)	ε_\perp (10^{-3})	D_\parallel (nm)	α_{tilt} (deg)
STO	0.4015	0.4021	2.8	3.0	0.0522	152	46.5	196	0.012
SLAO	0.4041	0.4004	7.6	-4.8	0.2003	50	12.7	55	0.447

perovskite heterostructures like $\text{SrTiO}_3/\text{SrRuO}_3/\text{Pb}(\text{Zr,Ti})\text{O}_3$ or $\text{SrRuO}_3/\text{GdScO}_3$, where the epitaxial strain induces local tilt/distortion of the RuO_6 octahedra or the formation of monoclinic distorted nanodomains.^{13,14}

In the present study, we make a careful analysis of strain and local lattice distortions in BCZT thin films with high dielectric and piezoelectric response and identify in the peculiar nanoscale features the cause of these enhancements. The results can be of more general relevance also for other materials with nanoscale fluctuations in constrained conditions.

2. EXPERIMENTAL SECTION

The ceramic targets used for the thin films deposition were fabricated by conventional solid-state method. Precise amounts of reagent-grade starting materials of BaCO_3 , CaCO_3 , TiO_2 and ZrO_2 were mixed for obtaining the stoichiometric composition of $(1-x)\text{Ba}(\text{Ti}_{0.8}\text{Zr}_{0.2})\text{O}_3 - x(\text{Ba}_{0.7}\text{Ca}_{0.3})\text{TiO}_3$, $x = 0.45$ (BCZT 45). The resulting targets were characterized using X-ray diffraction (XRD) technique. The XRD measurements were performed with a Panalytical X'Pert MRD system equipped with Pixcel detector, by using a monochromated beam ($\lambda \text{ Cu K}\alpha = 1.540598 \text{ \AA}$) provided by a hybrid asymmetric monochromator $2x\text{Ge}(220)$. The BCZT 45 targets show pure phase perovskite structure with rhombohedral $R\bar{3}m$ symmetry, as expected for this composition, and the pseudocubic lattice parameter was found to be $a = 4.0176 \text{ \AA}$.

Epitaxial thin films of BCZT 45 were obtained by pulsed laser deposition (PLD) technique. The deposition of the thin films has been carried out in oxygen atmosphere with partial pressure of 10 Pa, on substrates heated at 700 °C. For achieving the desired strain conditions two different single-crystal substrates, (001) SrTiO_3 (STO) and (001/100) SrLaAlO_4 (SLAO), have been selected. The thickness of the films was measured by spectrometric ellipsometry and confirmed by transmission electron microscopy (TEM) in cross section, being in the range of 160–175 nm.

The structural characterization of the BCZT thin films has been made by XRD on the same equipment used for the target characterization and by high-resolution transmission electron microscopy technique (HRTEM). Cross-section specimens for HRTEM investigations have been prepared by mechanical grinding and ion milling using a Gatan PIPS installation at 4 kV acceleration voltage and 7° beam incidence angle. The samples have been investigated on a JEOL ARM 200 F transmission electron microscope operated at 200 kV. For dielectric measurements Au interdigital electrodes (IDE) have been deposited on top surfaces of the films by employing the lift-off technique. The capacitance and dielectric loss have been measured at different temperatures and frequencies by using an HP4194A impedance analyzer.

The local piezoelectric properties, polarization dynamics and switching characteristics of the samples were investigated by Piezoresponse Force Microscopy (PFM), on a commercial AFM (XE-100, Park Systems). Two types of cantilevers were used: titanium–platinum coated NSC36 series (Mikromasch) for lower stiffness ($k < 1 \text{ N/m}$), and bulk platinum cantilevers (Rocky Mountain

Nanotechnology) with higher stiffness ($k \sim 18 \text{ N/m}$). The samples were glued to stainless steel disks with silver paint in order to achieve a good electrical contact. The conductive Nb-doped STO substrate acted as bottom electrode and the conductive AFM tip acted as top electrode. The DC bias was applied to the substrate and the AC (testing) bias was applied to the tip, both referenced to a common ground. The local vertical (out-of-plane) mechanical response of the material to the AC bias was recorded during topography scanning (PFM imaging) and during ramping of the DC bias (hysteresis loops). The amplitude and phase of the piezoelectric out-of-plane response were extracted from the AFM vertical deflection signal by a lock-in amplifier (Stanford Research Systems SR830).

3. RESULTS AND DISCUSSION

3.1. Structural Results. The XRD patterns of the BCZT/STO and BCZT/SLAO heterostructures are presented in Figure 1. Highly oriented (00l) growth of the BCZT films is observed on both substrates, in spite of the large lattice misfit between the pseudocubic lattice parameters of the BCZT 45 target ($a = 4.0176 \text{ \AA}$) and the STO ($a = 3.905 \text{ \AA}$) and SLAO ($a = 3.756 \text{ \AA}$) lattice parameters. The only peaks observed in the diffractograms are from the (00l) reflections indicating the absence of impurity phases or domains with other orientations, as can be better seen in Figure 1b, where only half of the recorded angular range is presented.

The 360° φ -scans of BCZT (101) and STO (101) asymmetric reflections (Figure 1c) and BCZT (101) and SLAO (103) reflections, respectively (Figure 1d) evidence perfectly matched 4-fold symmetries, suggesting a cube-on-cube epitaxial growth.

The in-plane and out-of-plane lattice parameters were determined by conventional and off-axis diffraction. The out-of-plane (a_n) lattice parameters were obtained in normal $\theta-2\theta$ scans using the formula $a_n = 2d_{002}$, while the in-plane (a_p) lattice parameters have been obtained by tilting the samples at 45° in a $\theta-2\theta$ scan from the equation

$$a_p = 2 / \sqrt{d_{202}^{-2} - d_{002}^{-2}} \quad (1)$$

where d_{002} and d_{202} are the lattice spacing of (002) and (202) planes, respectively.¹⁵

To separate the coherently diffracting domains effect from the lattice strain effect, we used the Williamson-Hall method on the (00l) reflections.¹⁶ The mathematical relation between the X-ray wavelength λ , integral breadth β (instrumental corrected FWHM), θ Bragg angle, the domain size (namely, the short coherence length perpendicular to the substrate surface) D_\perp and the vertical inhomogeneous strain (ε_\perp) is

$$\frac{\beta \cos \theta}{\lambda} = \frac{1}{D_{\perp}} + 4\varepsilon_{\perp} \frac{\sin \theta}{\lambda} \quad (2)$$

The plot of $(\beta \cos \theta / \lambda)$ versus $(\sin \theta / \lambda)$ gives the value of the strain from the slope and the vertical coherence length from the ordinate intercept.

The mosaicity of the films is described by the ω -scans of symmetric reflections. Figure 1e presents the superimposed ω -scans (so-called rocking curves) of the (002) reflection of the BCZT films deposited onto STO and SLAO substrates. The broadening of the ω -scans symmetric reflections is determined by the tilt angle α_{tilt} (rotation of the mosaic blocks around the axis lying in the substrate surface) and to the coherence length parallel to the substrate surface (D_{\parallel}). Due to the different dependences of the two broadening mechanisms on the reflections orders, a similar Williamson–Hall approach proposed by Mentzger et al.¹⁷ allows the separation of the two effects. By plotting $\beta_{\omega}(\sin \theta) / \lambda$ against $(\sin \theta) / \lambda$ where β_{ω} is the FWHM of the rocking curve, θ the Bragg angle and λ the X-ray wavelength, the tilt angle is obtained from the slope of the linear dependence and the lateral coherence length from the inverse of the intercept of the fitting line with the ordinate. The structural data extracted from the different X-ray diffraction results are presented in Table 1 and will be commented in the following.

The low magnification cross-sectional TEM images (Figure 2a,b) reveal the compact growth of the BCZT thin films deposited on the two different substrates (STO and SLAO). The BCZT layer grown on STO substrate shows a more compact structure and better interface than the film grown on SLAO, which contains structural defects (grain boundaries, threading and misfit dislocations), due to the higher misfit of the in-plane lattice parameters.

The selected area electron diffraction (SAED) patterns in Figure 2c,d indicate an epitaxial or highly orientated growth of the BCZT films with respect to the substrate in both analyzed cases. The main Miller index corresponding to the BCZT layer and the substrate (subscript s) are indicated on the diffraction patterns. The cube-on-cube growth can be noticed, with the following relationship between the layer and substrate main axes: [001] BCZT ||[001]s and [100] BCZT ||[100]s. The density of defects in the BCZT layers and the associated strain field revealed by the nanometric dark/bright stripes determines the slight elongation of the diffraction spots corresponding to the BCZT layer along a direction perpendicular to the one of the defects (parallel to the interface), unlike the diffraction spots of the substrates which do not exhibit any particular deformation.

The epitaxial growth is also confirmed by the HRTEM images at the film–substrate interface for both substrates, as can be seen in Figure 2e,f.

3.2. Microstrain Analysis. The residual strain in the as-grown layers has been measured on HRTEM micrographs using the geometrical phase analysis (GPA) software.¹⁸ A typical result concerning the strain mapping on a large area HRTEM image next to the BCZT/STO interface is presented in Figure 3 (a–c). The in-plane and out-of-plane lattice parameter variation, ε_{xx} and ε_{yy} , respectively, have been measured with respect to a reference area chosen inside the STO substrate. The ε_{xx} and ε_{yy} strain maps are represented in false colors in Figure 3b,c.

The corresponding quantitative values can be read out on the line profiles obtained along the black arrows across the

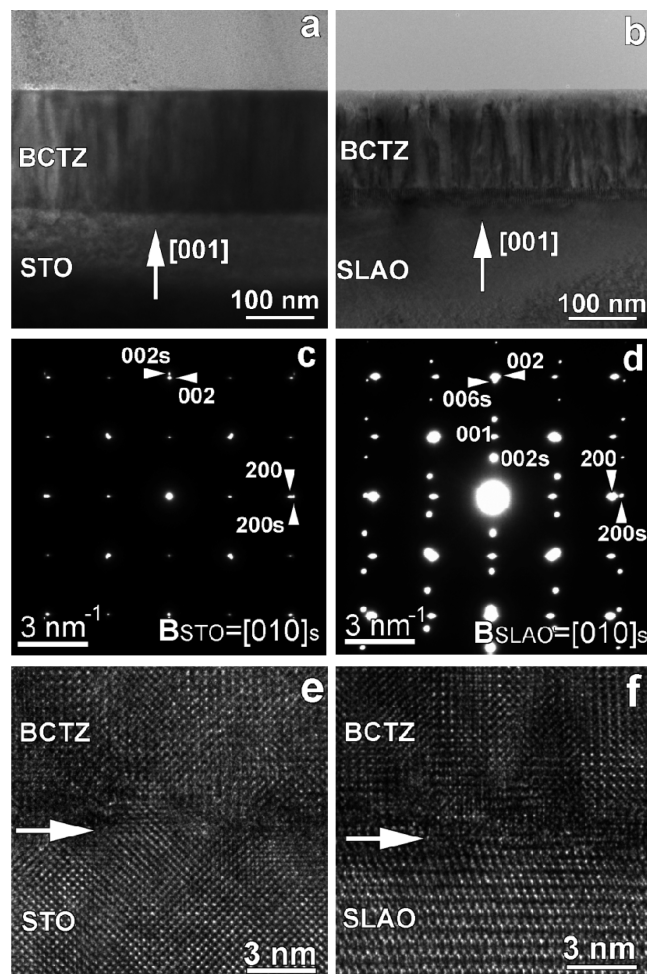


Figure 2. Low-magnification cross-section TEM images showing the BCZT layers grown on STO(001) (a) and SLAO(001) (b) single crystal substrates; (c) and (d) corresponding SAED patterns revealing epitaxial relationship between the as grown layers and the single crystal substrates; (e) and (f) corresponding HRTEM images at the film–substrate interface for the two substrates. The interface is marked by the white arrow.

interface, as indicated on the colored maps. In order to smooth out the intensity variations due to noise or presence of defects (strain field around dislocation cores), the line profile has been averaged on a lateral range around the black arrow (about 80 nm wide), as indicated by the dashed black line on the strain maps.

The ε_{xx} and ε_{yy} in-plane and out-of-plane strain profiles for the BCZT/STO film are shown in Figure 3d, in the upper and lower plots, respectively. In the analyzed micrographs, the line profiles have been averaged on a lateral range on the widest band allowed by the micrograph, such as a significant region of the substrate is included as reference in the measured (averaged) area. Small noise oscillations around zero are observed in the STO substrate region chosen as reference area. In the BCZT film region the line profile shows a jump to a plateau around the average value of $2.8 \pm 0.4\%$ for ε_{xx} and $2.9 \pm 0.3\%$ for ε_{yy} . Using these values and considering that the substrate lattice is fully relaxed (quasi-infinite thickness as compared to the BCZT thin film), we have calculated the average in-plane (a) and out-of-plane (c) lattice parameters inside the BCZT thin film, starting from the bulk values of the

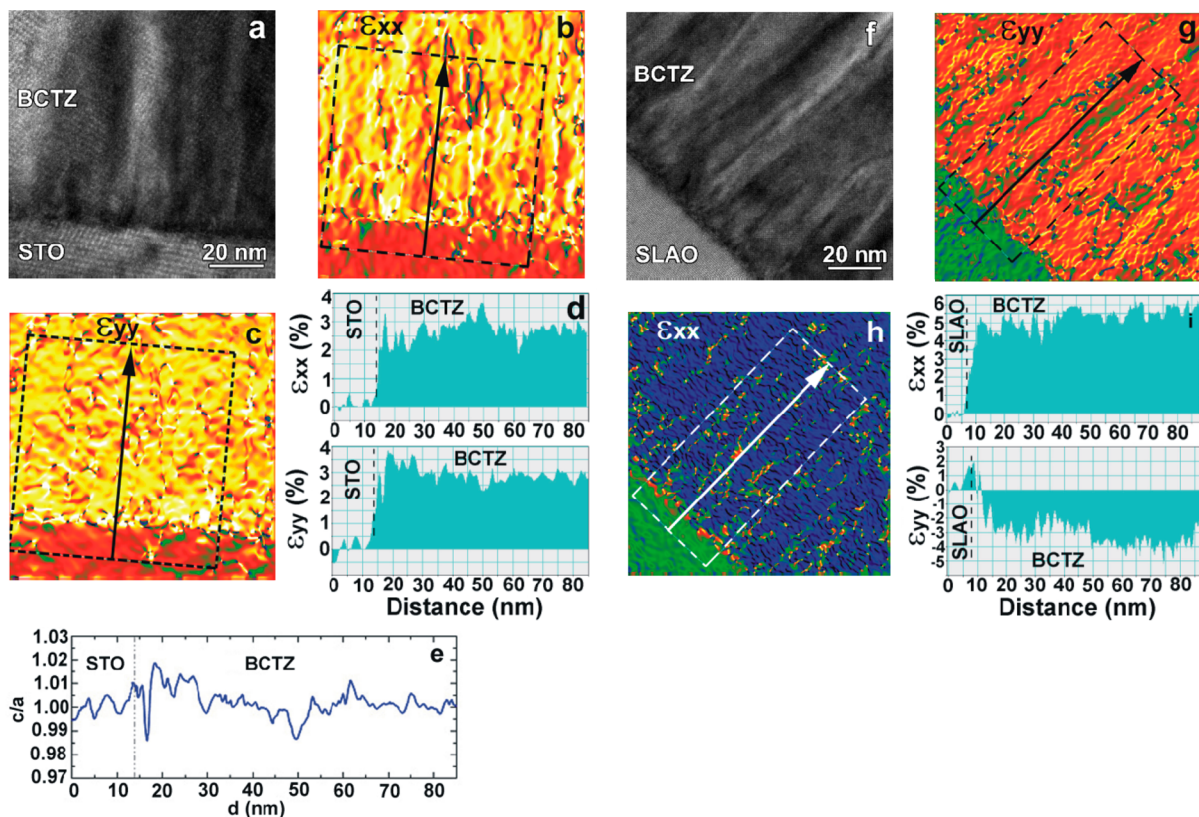


Figure 3. (a) Large-area HRTEM image at the BCZT/SRO interface. (b and c) 2D maps of in-plane and out-of-plane lattice parameter variation and residual strain, ϵ_{xx} and ϵ_{yy} , respectively. (d) Line profiles of the ϵ_{xx} and ϵ_{yy} maps along the arrow crossing the interface. (e) Tetragonality c/a ratio variation along the same line. (f) Large-area HRTEM image at the BCZT/SLAO interface. (g and h) 2D maps of in-plane and out-of-plane lattice parameter variation and residual strain, ϵ_{xx} and ϵ_{yy} , respectively. (i) Line profiles of the ϵ_{xx} and ϵ_{yy} maps along the arrow crossing the interface.

STO lattice parameter ($a_{\text{STO}} = 3.905 \text{ \AA}$). This method was originally applied to study the displacement and strain fields associated with domain walls in PbTiO_3 , which are defined by the relative directions of the a and c axis.¹⁸ The elastic and electric properties of the material are strongly influenced by the structure of the interfaces between domains, so it is important to determine how the tetragonality (c/a ratio) varies across the interface and how abruptly the distortion of the lattice occurs. In Figure 3e we have represented the tetragonality c/a variation along the BCZT film thickness. We recall that the lattice distortions in all the phases of BCZT are very small, as discussed in the Introduction, with $c/a \sim 1.005$ in T phase.² Thus, given the film thickness (175 nm), the lattice in the BCZT/STO film is almost completely relaxed to the bulk value. However, the tetragonality ratio fluctuations, clearly visible in Figure 3e, may be assimilated with a and c -axis interchanging in tetragonal nanodomains, with coexisting R or O nanodomains, or both. We presume that, as previously found in other epitaxial ferroelectric films¹² and discussed in the Introduction, the tetragonal T phase, originally induced by the epitaxial strain in very thin BCZT 45 films, evolve into a mixture of nanodomains of different phases close in energy when the film thickness increases.

Similar image processing has been applied to the HRTEM images obtained on the BCZT/SLAO films (Figure 3f–i). The in-plane and out-of-plane lattice parameters of BCZT have been calculated starting from the bulk values of the SLAO lattice parameters and using the quantitative data read out of the 2D strain maps of the cross-section HR micrographs. In the case of the SLAO substrate, we calculated the strain maps by

comparing the $(200)_{\text{BCZT}}$ and $(002)_{\text{BCZT}}$ film lattice fringes with the $(200)_s$ and $(006)_s$ substrate lattice fringes spaced at 0.186 and 0.210 nm, respectively. Unlike the film on the STO substrate, for the GPA calculation of the ϵ_{yy} strain field in BCZT/SLAO we have chosen as reference for the SLAO substrate the interplanar distance between the $(006)_s$ planes parallel to the interface, as this set of planes exhibits the nearest value to the $(002)_{\text{BCZT}}$ interplanar distance. We remember here that the two substrates, SrTiO_3 (STO) and SrLaAlO_4 (SLAO), have different crystalline structures. While STO is a cubic perovskite ($a = 3.905 \text{ \AA}$, S.G. $Pm3m$), SLAO has a tetragonal structure ($a = b = 3.755 \text{ \AA}$, $c = 12.62 \text{ \AA}$, S.G. $I4/mmm$). The pseudocubic lattice parameter of the deposited BCZT 45 layers is $a = 4.0176 \text{ \AA}$, about 3 times smaller than the c parameter of the SLAO substrate. For the out-of-plane strain in BCZT we have chosen to compare the interplanar distance between planes oriented parallel to the interface, both in BCZT and in the substrates. In addition, we have selected those families of planes having close values for the interplanar distance. Therefore, for the BCZT/STO sample we have chosen the $(002)_{\text{BCZT}}$ planes (measured interplanar distance ca. 2.01 Å) and $(002)_{\text{STO}}$ sets of planes (interplanar distance 1.95 Å), while for the BCZT/SLAO sample we have chosen the same $(002)_{\text{BCZT}}$ planes (measured interplanar distance 2.01 Å) for the film, but the $(006)_{\text{SLAO}}$ planes (interplanar distance 2.10 Å) for the SLAO substrate. On the SAED patterns the corresponding diffraction spots appear like slightly separated doublets, both in the STO and SLAO case.

Negative values of ϵ_{yy} have been measured inside the film area with respect to the SLAO substrate, as a result of the larger

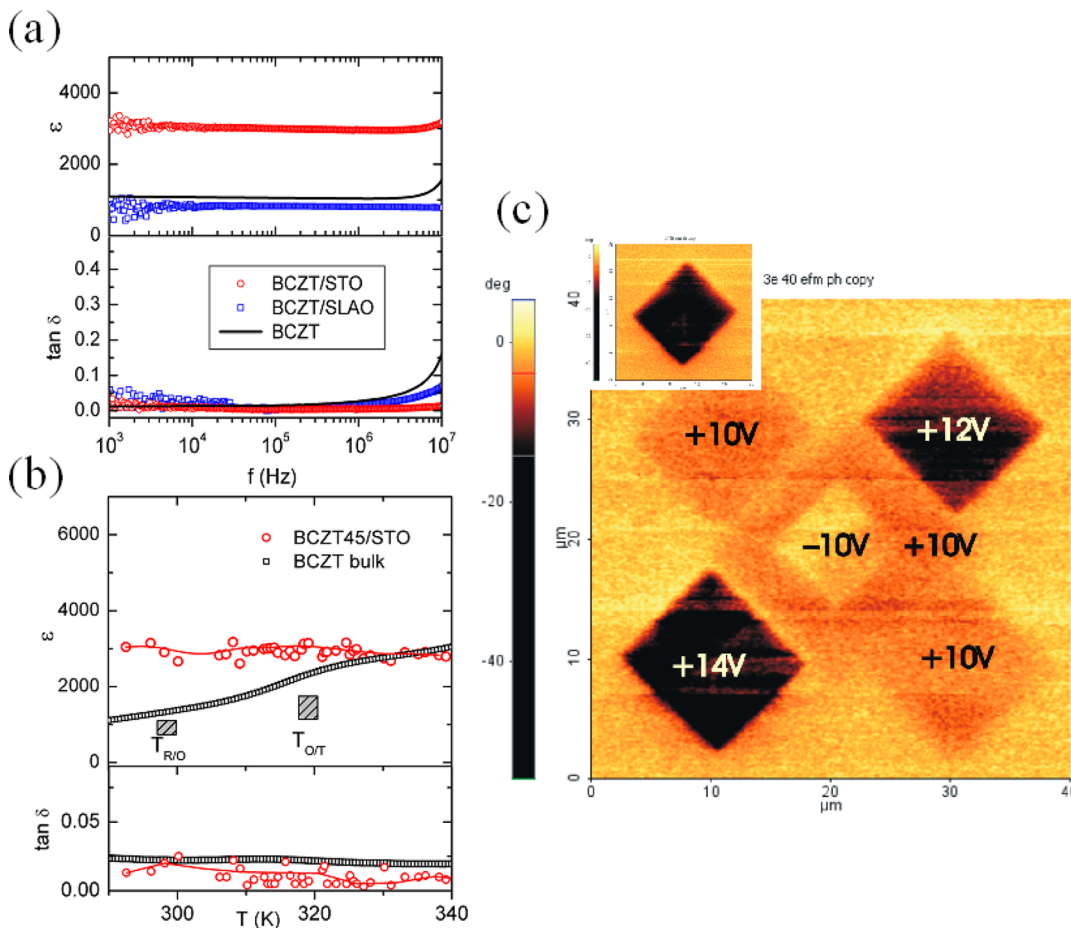


Figure 4. (a) BCZT/STO and BCZT/SLAO dielectric permittivity and loss values dependence on frequency at room temperature. Continuous curves represent the dielectric permittivity and loss values for the bulk BCZT sample. (b) Dielectric permittivity and loss variation with temperature of (○) BCZT/STO films and (□) bulk BCZT 45 samples. Hatched rectangles approximately indicate the R/O and O/T phase transformation regions in the bulk sample. (c) Out-of-plane PFM image for BCZT/STO thin films.

[006]_s interplanar distance in the SLAO substrate with respect to the [002]_{BCZT} interplanar distance in the thin film. The SLAO-BCZT interface exhibits a high density of dislocations characterized by their own strain field, generating a narrow band of tensile strain along the interface as indicated by the red stripe at the interface on the ϵ_{yy} map (positive values on the ϵ_{yy} line profile). Extended structural defects (threading dislocations and grain boundaries) are also present inside the BCZT/SLAO films, at a relatively higher density compared to the film deposited onto STO (Figures 2b and 3f). These defects modify the local stoichiometry and induce a local strain field, with likely consequences on the dielectric losses and the lower dielectric permittivity, as will be shown in the following.

The structural data extracted from XRD and HRTEM analysis are gathered in Table 1. An inspection of the data evidence the high crystallographic quality of the BCZT film deposited on STO, with a vertical coherence length D_{\perp} of 152 nm, close to the film thickness (175 nm) as determined by TEM. Extremely low mosaicity, small broadening of the rocking curves (high parallel coherence length $D_{||}$) and, in particular, an extremely small value of the tilt angle can also be observed. The out-of-plane and in-plane lattice parameters are quite close to the values provided by TEM, which stands for the high homogeneity of the film. Instead, for the film deposited on SLAO substrate, much higher values for the broadening of the rocking curves, shorter vertical and parallel coherence lengths,

and substantially higher value of the tilting angle are measured, due to the large misfit with the substrate. Therefore, the structural quality of the BCZT/SLAO film is much lower, and we expect it to reflect in the dielectric properties.

3.3. Dielectric Permittivity and Piezoelectric Response. The dielectric permittivity of the film samples has been evaluated by using gold interdigital electrodes (IDE) deposited on the film surface. Dielectric spectroscopy measurements have been carried out between 1 kHz and 10 MHz on IDE structures consisting of $N = 21$ finger pairs of length $L = 464 \mu\text{m}$ and width $10 \mu\text{m}$. The interspace between fingers is $10 \mu\text{m}$, and thus, the distance D between finger centers is $20 \mu\text{m}$. The measurements yield the capacitance and the dielectric loss $\tan \delta$.

The in-plane dielectric constants of the Au/BCZT/STO and Au/BCZT/SLAO thin film capacitors with IDE configuration have been calculated by using the analytical model proposed in refs 20 and 21, which give for the dielectric constant of the thin film ϵ the following formula

$$\epsilon = \epsilon_s + \frac{C_n - C_K(1 + \epsilon_s)}{C_K(1 - \exp(-4.6h/D))} \quad (3)$$

where ϵ_s is the dielectric constant of the substrate, h is the film thickness, C_n is the measured capacitance of the IDE structure normalized to the finger length (L) and to the number of

fingers ($2N - 1$), while C_K is a constant depending on IDE geometry. In the case of IDE patterns with equal finger width and spacing, $C_K = 4.53 \text{ pF/m}$.^{19,20} The dielectric constant of the STO substrate is ~ 300 and that of the SLAO substrate is ~ 17 . The BCZT/STO and BCZT/SLAO dielectric constants and loss values dependence on frequency at room temperature are plotted in Figure 4a.

For comparison, the bulk dielectric permittivity and loss values are plotted, too. Very high values of dielectric permittivity (>3000) combined with very low dielectric loss (<0.01) are obtained for BCZT 45 film deposited on STO substrate, while lower dielectric permittivity value, comparable with that of the bulk material, has been obtained for BCZT/SLAO film. The differences in the dielectric permittivity values of the two films are attributed to their different structural quality. Thus, as it has been shown in the previous sections, the BCZT/SLAO interface shows a high density of dislocations, due to the high lattice misfit of the two materials. Moreover, a higher amount of extended structural defects (threading dislocations and grain boundaries) are present inside the BCZT/SLAO films in comparison with BCZT/STO films. The lower structural quality of BCZT/SLAO films was evidenced also by the higher values of the broadening of the rocking curves, shorter vertical and parallel coherence lengths, as well as substantially higher value of the tilting angle (Table 1), and it is associated with the higher dielectric losses and the lower dielectric permittivity values of these samples. The occurrence of many defects and dislocations has a detrimental effect on the dielectric response because they pin the nanodomain walls and do not allow the easy movement of walls. This is manifested also in the higher losses for BCZT/SLAO film.

We mention that the in-plane dielectric constant values have been measured on a large number of capacitors on each sample; therefore, they can be considered as representative for each configuration. Moreover, to verify the experimental and calculation methods, we repeated the measurements on IDE electrodes directly deposited on the STO and SLAO substrates. The same model has been used to calculate their dielectric constants. Perfect agreement has been obtained between the measured and the data sheet values of the STO and SLAO dielectric constants.

We mention also that, although dielectric results have been occasionally reported on some BCZT films,^{21–25} they show lower values or they are accompanied by substantial variation with frequency, which is a fingerprint of some relaxation mechanism contribution to permittivity, while the values reported here on BCZT/STO film show neglectable variation up to 10 MHz. A comparison with other BCZT films as well as with other lead-free ferroelectric films is given in a table in the Supporting Information.

The dielectric permittivity and loss variation with temperature of BCZT/STO films have been measured and compared with similar curves obtained on bulk BCZT 45 samples (Figure 4b).

In the calculation, we have taken into account the variation with temperature of the dielectric constant of the substrate (Supporting Information). The fact that the film values do not follow the increasing with temperature of bulk values can be explained in the following way: the increasing with T of bulk values is due to the increased mobility of polar domains on approaching ferroelectric-paraelectric transition, which for bulk BCZT is about 365 K.⁴ However, in epitaxial thin films, T_c is usually higher than in bulk, therefore this increasing on

approaching the transition temperature will occur at higher temperatures than in bulk. However, we could not measure the in-plane dielectric constant at higher T due to the peculiar holder type for contacting interdigital electrodes which does not support higher temperature.

It can be observed that the dielectric constant of the film preserves a high value in all the temperature region. It does not show the anomalies associated with R–O and O–T transitions in bulk. Instead ϵ conserves a high value (~ 3000) in a large temperature range, well above room temperature. This behavior is associated with the broad coexistence range of T, O and R phases, which probably extends up to higher temperatures in thin films. As discussed in the Introduction, when the epitaxial strain is partially released by increasing film thickness, the induced tetragonal phase evolves into a nanoscale mixture of T, O, and R-like nanodomains. Therefore, we propose as possible origin of the high dielectric response the intrinsic contribution of the nanoscale boundaries.⁸ Indeed, as confirmed by a rich phenomenology, phase boundaries in solids have been found to influence critically the macroscopic properties of materials.^{8,12} Near the phase boundary the free energies of different competing phases are almost degenerate, producing a nearly continuous variation in the local structure from phase to phase. As a consequence, a small external signal can induce a high response in such a material.¹²

It is well established also that in polar materials the difference between the free energies of the competing phases near the phase boundary decreases and vanishes when approaching it.²⁶ In this limit, the ferroelectric material can behave as a dipolar glass,²⁶ where the polarization is only weakly coupled with the lattice. The difference between the free energies of the phases strongly reduces so that small perturbations like structural defects, chemical fluctuations, or small strains in films can lead to phase instabilities. This finally leads to the deviation of polarization from the easy directions within the ferroelectric domains of T, R, and O phases and to the formation of frustrated nanodomains.²⁶ Thus, the high dielectric permittivity of BCZT thin films can be seen as a loss of rotation stability of the polarization associated with the presence of nanodomains. This results in a divergence of fluctuations of polarization direction and a peak of dielectric susceptibility.²⁶

Moreover, an enhanced field-induced rearrangement of nanodomains under applied field, caused by a drastic reduction of the polar anisotropy and leading to a high piezoresponse, should be also measured on such configurations. This is indeed what we have observed in BCZT/STO thin films, from the out-of-plane piezoelectric response (PFM image) and switching kinetics tested at different applied electric DC fields. An example of PFM imaging is shown in Figure 4c. Square shaped domains were first “written” on the material by applying a DC bias between the substrate and the tip held at ground potential, during topography scanning. The piezoelectric response was subsequently “read” by applying a 3 V, 10 kHz AC bias on the tip while holding the substrate at ground potential. The switching behavior has been tested at different DC bias values and orientation. The domains in Figure 4c correspond to the following values of the DC bias: upper left and lower right ($10 \times 10 \mu\text{m}$), + 10 V; center ($15 \times 15 \mu\text{m}$, dark), + 10 V; center ($7 \times 7 \mu\text{m}$, light), - 10 V; upper right and lower left ($10 \times 10 \mu\text{m}$), + 12 V and +14 V, respectively. In the inset image, a square shaped domain written on the BCZT thin film by applying +15 V DC bias is presented. The $0\text{--}180^\circ$ reversibility of the out-of-plane piezoelectric response evidences a net out-

of-plane switchable polarization which is correlated with the applied DC bias values and orientation, the upward polarization state being obtained for positive electric field and easily reversed by changing the field orientation.

4. CONCLUSIONS

In summary, lead-free ferroelectric BCZT 45 thin films have been grown epitaxially on (001) (STO) and (001/100) (SLAO) single-crystalline substrates by pulsed laser deposition. The epitaxial growth of the films has been confirmed by X-ray diffraction and HRTEM. A microstrain analysis and the variation of the in-plane and out-of-plane lattice parameters on different areas has been evidenced by GPA performed on HRTEM images. A nanoscale level tetragonality ratio variations, associated with the existence of polar nanodomains was evidenced on the BCZT/STO films which have a high structural quality. The in-plane dielectric permittivity showed very high values (>3000) for the BCZT film deposited on STO substrate, in a wide frequency range. This has been attributed to the loss of rotation stability of the polarization associated with the presence of nanodomains, which results into a divergence of fluctuations of polarization direction and a peak of dielectric susceptibility.

■ ASSOCIATED CONTENT

Supporting Information

The Supporting Information is available free of charge on the ACS Publications website at DOI: [10.1021/acsami.5b06745](https://doi.org/10.1021/acsami.5b06745)

Dielectric constant and loss of used substrates, temperature dependence of SrTiO₃ dielectric constant, comparison with similar results reported on lead-free ferroelectric films, and references. ([PDF](#))

■ AUTHOR INFORMATION

Corresponding Author

*E-mail: nicu.scarisoreanu@inflpr.ro. Fax: 0040214574467.

Notes

The authors declare no competing financial interest.

■ ACKNOWLEDGMENTS

N.D.S. and V.I. gratefully acknowledge the financial support from UEFISCDI in the frame of the TE14/2013 PNII-RU-TE-2012-3-0467 project. C.G. and R.F.N. gratefully acknowledge the financial support from UEFISCDI in the frame of the PN-II-ID-PCE-2012-4-0362 project.

■ REFERENCES

- (1) Kalyani, A. K.; Senyshyn, A.; Ranjan, R. Polymorphic Phase Boundaries and Enhanced Piezoelectric Response in Extended Composition Range in the Lead Free Ferroelectric BaTi_{1-x}ZrxO₃. *J. Appl. Phys.* **2013**, *114*, 014102–014102–6.
- (2) Fu, D.; Kamai, Y.; Sakamoto, N.; Wakiya, N.; Suzuki, H.; Itoh, M. Phase Diagram and Piezoelectric Response of (Ba_{1-x}Cax)(Zr_{0.1}Ti_{0.9})O₃ Solid Solution. *J. Phys.: Condens. Matter* **2013**, *25*, 425901–425905.
- (3) Keeble, D. S.; Benabdallah, F.; Thomas, P. A.; Maglione, M.; Kreisel, J. Revised Structural Phase Diagram of (Ba_{0.7}Ca_{0.3}TiO₃)-(BaZr_{0.2}Ti_{0.8}O₃). *Appl. Phys. Lett.* **2013**, *102*, 092903–092903–5.
- (4) Cordero, F.; Craciun, F.; Dinescu, M.; Scarisoreanu, N. D.; Galassi, C.; Schranz, W.; Soprunguk, V. Elastic Response of (1-x)Ba(Ti_{0.8}Zr_{0.2})O₃ – x(Ba_{0.7}Ca_{0.3})TiO₃ (x = 0.45–0.55) and the Role of the Intermediate Orthorhombic Phase in Enhancing the Piezoelectric Coupling. *Appl. Phys. Lett.* **2014**, *105*, 232904–232904–5.
- (5) Zhang, L.; Zhang, M.; Wang, L.; Zhou, C.; Zhang, Z.; Yao, Y.; Zhang, L.; Xue, D.; Lou, X.; Ren, X. Phase Transitions and the Piezoelectricity Around Morphotropic Phase Boundary in Ba-(Zr_{0.2}Ti_{0.8})O_{3-x}(Ba_{0.7}Ca_{0.3})TiO₃ Lead-Free Solid Solution. *Appl. Phys. Lett.* **2014**, *105*, 162908–162908–5.
- (6) Damjanovic, D.; Biancoli, A.; Batooli, L.; Vahabzadeh, A.; Trodahl, J. Elastic, Dielectric, and Piezoelectric Anomalies and Raman Spectroscopy of 0.5Ba(Ti_{0.8}Zr_{0.2})O₃–0.5(Ba_{0.7}Ca_{0.3})TiO₃. *Appl. Phys. Lett.* **2012**, *100*, 192907–192907–4.
- (7) Gao, J.; Zhang, L.; Xue, D.; Kimoto, T.; Song, M.; Zhong, L.; Ren, X. Symmetry Determination on Pb-free Piezoceramic 0.5Ba-(Zr_{0.2}Ti_{0.8})O₃–0.5(Ba_{0.7}Ca_{0.3})TiO₃ Using Convergent Beam Electron Diffraction Method. *J. Appl. Phys.* **2014**, *115*, 054108–054108–5.
- (8) Guo, H.; Voas, B. K.; Zhang, S.; Zhou, C.; Ren, X.; Beckman, S. P.; Tan, X. Polarization Alignment, Phase Transition, and Piezoelectricity Development in Polycrystalline 0.5Ba(Zr_{0.2}Ti_{0.8})O₃–0.5(Ba_{0.7}Ca_{0.3})TiO₃. *Phys. Rev. B: Condens. Matter Mater. Phys.* **2014**, *90*, 014103.
- (9) Fu, D.; Itoh, M.; Koshihara, S.; Kosugi, T.; Tsuneyuki, S. Anomalous Phase Diagram of Ferroelectric (Ba,Ca)TiO₃ Single Crystals with Giant Electromechanical Response. *Phys. Rev. Lett.* **2008**, *100*, 227601.
- (10) Hayward, S. A.; Salje, E. K. H. The Pressure–Temperature Phase Diagram of BaTiO₃: a Macroscopic Description of the Low-Temperature Behavior. *J. Phys.: Condens. Matter* **2002**, *14*, L599–604.
- (11) Liu, Z. K.; Li, X.; Zhang, Q. M. Maximizing the Number of Coexisting Phases near Invariant Critical Points for Giant Electrocaloric and Electromechanical Responses in Ferroelectrics. *Appl. Phys. Lett.* **2012**, *101*, 082904–082904–4.
- (12) Zhang, J. X.; Zeches, R. J.; He, Q.; Chu, Y. H.; Ramesh, R. Nanoscale Phase Boundaries: a New Twist to Novel Functionalities. *Nanoscale* **2012**, *4*, 6196–6204.
- (13) Aso, R.; Kan, D.; Shimakawa, Y.; Kurata, H. Atomic Level Observation of Octahedral Distortions at the Perovskite Oxide Heterointerface. *Sci. Rep.* **2013**, *3*, 2214–2220.
- (14) Ghica, C.; Negrea, R. F.; Nistor, L. C.; Chirila, C. F.; Pintilie, L. Nanoscale Monoclinic Domains in Epitaxial SrRuO₃ Thin Films Deposited by Pulsed Laser Deposition. *J. Appl. Phys.* **2014**, *116*, 023516–023516–11.
- (15) Specht, E. D.; Christen, H. M.; Norton, D. P.; Boatner, L. A. X-Ray Diffraction Measurement of the Effect of Layer Thickness on the Ferroelectric Transition in Epitaxial KTaO₃/KNbO₃Multilayers. *Phys. Rev. Lett.* **1998**, *80*, 4317–4320.
- (16) Williamson, G. K.; Hall, W. H. X-Ray Line Broadening from Filed Aluminium and Wolfram. *Acta Metall.* **1953**, *1*, 22–31.
- (17) Metzger, T.; Hopler, R.; Born, E.; Ambacher, O.; Stutzmann, M.; Stömmer, R.; Schuster, M.; Göbel, H.; Christiansen, S.; Albrecht, M.; Strunk, H. P. Defect Structure of Epitaxial GaN Films Determined by Transmission Electron Microscopy and Triple-Axis X-Ray Diffractometry. *Philos. Mag. A* **1998**, *77*, 1013–1025.
- (18) Hýtch, M. J.; Snoeck, E.; Kilaas, R. Quantitative Measurement of Displacement and Strain Fields from HREM Micrographs. *Ultra-microscopy* **1998**, *74*, 131–146.
- (19) Farnell, G. W.; Cermak, I. A.; Silverster, P.; Wong, S. K. Capacitance and Field Distributions for Interdigital Surface-Wave Transducers. *IEEE Trans. Sonics Ultrason.* **1970**, *SU-17*, 188–195.
- (20) Al-Shareef, H. N.; Dimos, D.; Raymond, M. V.; Schwartz, R. W.; Mueller, C. H. Tunability and Calculation of the Dielectric Constant of Capacitor Structures With Interdigital Electrodes. *J. Electroceram.* **1997**, *1*, 145–153.
- (21) Piorra, A.; Petraru, A.; Kohlstedt, H.; Wuttig, M.; Quandt, E. Piezoelectric Properties of 0.5(Ba_{0.7}Ca_{0.3}TiO₃) – 0.5[Ba-(Zr_{0.2}Ti_{0.8})O₃] Ferroelectric Lead-Free Laser Deposited Thin Films. *J. Appl. Phys.* **2011**, *109*, 104101–104101–4.
- (22) Lin, Y.; Wu, G.; Qin, N.; Bao, D. Structure, Dielectric, Ferroelectric, and Optical Properties of (1-x)Ba(Zr_{0.2}Ti_{0.8})O₃ –

$x(Ba0.7Ca0.3)TiO_3$ Thin Films Prepared by Sol–Gel Method. *Thin Solid Films* **2012**, *520*, 2800–2804.

(23) Kang, G.; Yao, K.; Wang, J. $(1 - x)Ba(Zr0.2Ti0.8)O_3 - x(Ba0.7Ca0.3)TiO_3$ Ferroelectric Thin Films Prepared from Chemical Solutions. *J. Am. Ceram. Soc.* **2012**, *95*, 986–991.

(24) Luo, B. C.; Wang, D. Y.; Duan, M. M.; Li, S. Growth and Characterization of Lead-Free Piezoelectric $BaZr0.2Ti0.8O_3 - Ba0.7Ca0.3TiO_3$ Thin Films on Si Substrates. *Appl. Surf. Sci.* **2013**, *270*, 377–381.

(25) Luo, B. C.; Wang, D. Y.; Duan, M. M.; Li, S. Orientation-Dependent Piezoelectric Properties in Lead-Free Epitaxial $0.5BaZr0.2-Ti0.8O_3 - 0.5Ba0.7Ca0.3TiO_3$ Thin Films. *Appl. Phys. Lett.* **2013**, *103*, 122903–122903–5.

(26) Khachaturyan, A. G. Ferroelectric Solid Solutions with Morphotropic Boundary: Rotational Instability of Polarization, Metastable Coexistence of Phases and Nanodomain Adaptive States. *Philos. Mag.* **2010**, *90*, 37–60.